D. A. Gómez-Gualdrón, C. M. Simon, W. Lassman, D. Chen, R. L. Martin, M. Haranczyk, O. K. Farha, B. Smit, and R. Q. Snurr, Impact of the strength and spatial distribution of adsorption sites on methane deliverable capacity in nanoporous materials Chem Eng Sci 159, 18 (2017) http://dx.doi.org/10.1016/j.ces.2016.02.030

Impact of the strength and spatial distribution of adsorption sites on methane deliverable capacity in nanoporous materials

Diego A. Gomez-Gualdron,[a] *Cory Simon,*[b] *William Lassman,*[a] *David Chen,*[a] *Richard L. Martin,*[c,d] *Maciej Haranczyk,*[c] *Omar K. Farha,*[e,f] *Berend Smit,*[b] *Randall Q. Snurr.*[a*]

[a] Department of Chemical and Biological Engineering, Northwestern University, 2145 Sheridan Road, Evanston, IL 60208, USA

[b] Department of Chemical and Biomolecular Engineering, University of California, Berkeley, Berkeley, CA 94709, USA

[c] Computational Research Division Lawrence Berkeley National Laboratory, Berkeley, CA 94720, USA

[d]Watson Group, IBM Almaden Research Centre, San Jose, CA 95210, USA

[e] Department of Chemistry, Northwestern University, 2145 Sheridan Road, Evanston, IL 60208, USA

[f] Department of Chemistry, Faculty of Science, King Abdulaziz University, Jeddah 22254, Saudi Arabia

***Corresponding Author**

E-mail: snurr@northwestern.edu

ABSTRACT:

The methane deliverable capacity of adsorbent materials is a critical performance metric that will determine the viability of using adsorbed natural gas (ANG) technology in vehicular applications. ARPA-E recently set a target deliverable capacity of 315 cc(STP)/cc that a viable adsorbent material should achieve to yield a driving range competitive with incumbent fuels. However, recent computational screening of hundreds of thousands of materials suggests that the target is unattainable. In this work, we aim to determine whether the observed limits in deliverable capacity (~200 cc(STP)/cc) are fundamental limits arising from thermodynamic or material design constraints. Our efforts focus on simulating methane adsorption isotherms in a large number of systems, resulting in a broad exploration of different combinations of spatial distributions and energetics of adsorption sites. All systems were classified into five adsorption scenarios with varying degrees of realism in the manner that adsorption sites are created and endowed with energetics. The scenarios range from methane adsorption on discrete idealized lattice sites to adsorption in metal-organic frameworks with coordinatively unsaturated sites (CUS) provided by metalated catechol groups. Our findings strongly suggest that the ARPA-E target is unattainable, although not due to thermodynamic constraints but due to material design constraints. On the other hand, we also find that the currently observed deliverable capacity limits may be moderately surpassed. For instance, incorporation of CUS in **IRMOF-10** is predicted to yield a 217 cc(STP)/cc deliverable capacity. The modified material has a ~0.85 void fraction and a heat of adsorption of ~15 kJ/mol. This suggests that similar, moderate improvements over existing materials could be achieved as long as CUS incorporation still maintains a relatively large void fraction. Nonetheless, we conclude that more significant

improvements in deliverable capacity will require changes in the currently proposed operation conditions.

KEYWORDS: gas storage, molecular simulation, metal-organic frameworks, open metal sites, dispersion interactions

1. INTRODUCTION

A widely abundant resource, natural gas (NG) has attracted much attention as a bridging fuel in the transition to clean and renewable energy sources, for instance, in vehicular applications. Compared to gasoline, natural gas produces less carbon dioxide per unit of energy released during combustion. However, although natural gas and gasoline have a similar energy per unit mass, the former has a significantly smaller energy per unit volume at ambient conditions. Consequently, NG must be densified to be stored onboard the vehicle in a reasonably sized fuel tank. Current NG-powered passenger vehicles use compressed natural gas (CNG), which is stored at ~250 bar in thick-walled and therefore heavy and expensive, non-conformable on-board tanks. The CNG refill stations require expensive multi-stage compressors to achieve ~250 bar in an energy-intensive process. Through adsorption, porous materials can significantly increase the density of natural gas while utilizing lower storage pressures, and therefore their use in adsorbed natural gas (ANG) tanks has been considered a promising alternative to reduce infrastructure costs and tank design constraints (Eddaoudi et al., 2002, Düren et al., 2004;; Ma et al., 2007; Zhou et al., 2007, Ma and Zhou, 2010; Wu et al., 2009). A critical performance metric for such porous materials is the *deliverable capacity*, which is the difference between the amount of gas adsorbed at the storage pressure and at the discharge pressure (Gándara et al., 2014; Li et al., 2014; Wilmer et al., 2013). The deliverable capacity is a metric for the driving range on a full

fuel tank since it takes into account the stranded gas that remains in the adsorbent when the ANG tank cannot provide a sufficient flow rate to the engine and is thus seemingly depleted.

ARPA-E has recently established a target in which an ANG tank should match the performance of a CNG tank, although operating at lower pressures. Specifically, the ANG tank should have a deliverable capacity of 9.2 MJ/L between 65 bar (storage) and 5.8 bar (depletion), at room temperature (ARPA-E, 2012). Nevertheless, since it is estimated that an adsorbent material can be packed within the tank with at most a ~75% packing efficiency, the target for the deliverable capacity of the adsorbent material itself is 12.5 MJ/L, or equivalently 315 cc(STP)/cc in terms of methane. Pursuing the ARPA-E target, a number of porous materials have been synthesized and evaluated experimentally (Barin et al., 2014; Gándara et al., 2014; Gómez-Gualdrón et al., 2014a; Grunker et al., 2014; He et al., 2013; Li et al., 2014; Mason et al., 2014; Peng et al., 2013; Wen et al., 2014) and/or via molecular simulation (Chung et al., 2014; Gómez-Gualdrón et al., 2014a; Martin et al., 2013; Sezginel et al., 2015). Furthermore, the rapid screening of materials by simulation methods has enabled the evaluation of thousands of hypothetical porous materials such as porous polymer networks (PPNs) (Martin et al., 2014b), zeolites (Simon et al., 2014), metal-organic frameworks (MOFs) (Gómez-Gualdrón et al., 2014b), and covalent organic frameworks (COFs) (Martin et al., 2014a). Figure 1 summarizes simulated and experimentally measured methane deliverable capacities (between 65 and 5.8 bar) for over 100,000 hypothetical MOFs and the current best synthesized MOFs versus the corresponding heat of adsorption (which is one of the properties that impacts deliverable capacity).

According to simulations (Figure 1), the best materials have deliverable capacities that improve ~250% upon the deliverable capacity of an adsorbent-free tank operating at identical

conditions (between 65 bar and 5.8 bar). Nevertheless, the best materials perform only at ~65% of the ARPA-E target. A reported thermodynamic ANG tank model (Zhang et al., 2015) predicts that at the proposed operation conditions and using a ~40 gallon tank, the best materials would allow for a driving range of ~150 miles. One potential solution to improve performance is to alter the operation conditions. For instance, waste heat from the engine could be redirected to the ANG tank to raise the delivery temperature to drive out the stranded gas (Fu et al., 2015; Gómez-Gualdrón et al., 2014b; Rana et al., 2014; Zhang et al., 2015). This possibility was also discussed in a recent large-scale multi-institutional computational study (Simon et al., 2015) in the context of the *Materials Genome Initiative*, where none of the hundreds of thousands of computationally screened porous materials reached the ARPA-E target without raising the delivery temperature.

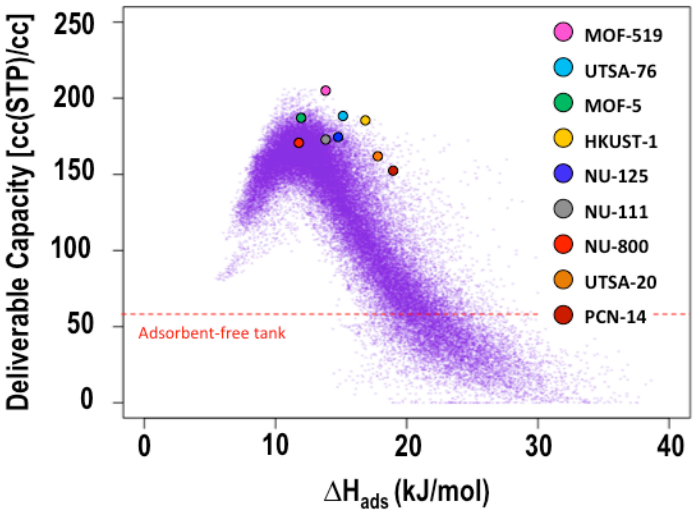

Figure 1. Methane adsorption data from the literature. Simulated and experimental volumetric deliverable capacity between 65 and 5.8 bar of ~120,000 hypothetical MOFs (purple points, simulation data) and top synthesized MOFs (colored labeled points, experimental data) versus heat of adsorption (ΔH_{ads}). Values are taken from Gómez-Gualdrón et al. (2014b) for hypothetical MOFs, Peng et al. (2013) for NU-125, NU-111, HKUST-1, UTSA-20, and PCN-14, Mason et al. (2014) for MOF-5, Li et al. (2014) for UTSA-76, Gómez-Gualdrón et al. (2014a) for NU-800, and Gándara et al. (2014) for MOF-519. (Note that the reported pore volume for MOF-519 is higher than the maximum pore volume computationally calculated for the reported MOF-519 crystallographic structure, which suggests that the reported MOF-519 density used to convert measured gravimetric loadings to volumetric loadings may be incorrect.) As reference, the horizontal line represents the deliverable capacity between 65 and 5.8 bar of the adsorbent-free tank.

Materials that have been created and evaluated computationally have been inspired by pre-existing material designs. This is similar to what occurs in experimental efforts. For instance, MOF synthesis strategies are often based on functionalization (Eddaoudi et al., 2002; Kim and Cohen, 2012) and/or isoreticular expansion (Barin et al., 2014; Cavka et al., 2008; Eddaoudi et al., 2002; Furukawa et al., 2011; Wang et al., 2015; Yuan et al., 2010) of "parent" MOF structures. On these grounds, before considering changes in operation conditions as the most suitable alternative, it is critical to determine whether the observed limits in deliverable capacity at room temperature after the screening of a large number of materials are *fundamental* limits arising from thermodynamic or material constraints, where the former cannot be surpassed even if more radical material designs could be achieved. In this work, our goal is to probe into such methane adsorption limits at operation conditions specific to the above-mentioned ARPA-E target. We do so using molecular simulation to explore different strategies to provide adsorption sites with varying spatial distributions and energetics for methane adsorption and observing the impact on methane deliverable capacity. The different spatial distributions and energetics of sites can be classified into five hypothetical scenarios, where the realistic character of each scenario varies in terms of i) the "material penalty" to create adsorption sites and ii) the adsorption energy characteristics of the sites.

2. COMPUTATIONAL METHODS

We performed grand canonical Monte Carlo (GCMC) simulations at the pressures of interest to calculate methane adsorption loadings at 298 K in all investigated systems. In all simulations, we implemented periodic boundary conditions and modeled methane molecules as Lennard-Jones spheres with parameters from the TraPPE force field (Martin and Siepmann, 1998). This force field was parameterized to reproduce experimental phase equilibrium data for methane.

Despite its simplicity, the TraPPE methane model has been proven effective in reproducing methane adsorption data. Indeed, Rana et al. (2014) recently showed that the TraPPE methane model outperforms five-site methane models (Chen and Siepmann, 1999; Sun et al., 1992, Lucena et al., 2010) in reproducing experimental methane adsorption data in M-MOF-74 variants. We used a cutoff radius of 12.8 Å to truncate pair-wise interactions. We utilized the Peng-Robinson equation of state to relate the gas-phase pressure and temperature of methane to its respective chemical potential.

In Section 3.1 (scenario 1), we built a series of FCC-arranged "pockets" with varying distances *d* between the pocket centers. In this spatially discrete model, methane molecules are confined to reside in the volume of each pocket, and each pocket is allowed to hold one methane molecule at most. We then endowed each pocket with an energy U_o if occupied by a methane molecule and zero otherwise. In Section 3.2 (scenario 2), we endowed all of space with a background energy U_o and allowed methane molecules to freely explore spatial configurations. In scenario 1, we attempted insertions and deletions of methane molecules at the lattice voxels. In scenario 2, we attempted insertions, deletions, and translations of methane molecules. For these simulations, we used C++ codes that are publicly available on GitHub (Simon, 2015). Further details are provided in the Supplementary Information.

In Sections 3.3 through 3.5 we investigated adsorbent system models that were created using the Crystal Builder module of Materials Studio (Accelrys Inc., 2001-2011). GCMC simulations for these structures were done using the simulation code RASPA (Dubbeldam et al., 2016). We performed 10,000 cycles for initialization and 10,000 cycles for statistics collection. A cycle corresponds to N Monte Carlo moves, where N is the number of molecules in the simulation supercell (or 20 if $N < 20$). Insertion, deletion, and translation moves of adsorbate atoms were

performed with equal probabilities, whereas atoms of the structures were held fixed during simulations.

The Lennard Jones (LJ) parameters for the interactions between methane molecules and adsorbent (pseudo)atoms were obtained applying the Lorentz-Berthelot mixing rules (Allen and Tildesley, 1990) to the parameters of methane (TraPPE force field) (Martin and Siepmann, 1998) and the adsorbent (pseudo)atoms (Universal force field, UFF) (Rappe et al., 1992). As discussed in Sections 3.3 through 3.4, the LJ ε parameters of adsorbent (pseudo)atoms were artificially modified to reproduce different methane-(pseudo)atom interaction strengths. Similarly, in section 3.5, we systematically modified the parameters of coordinatively unsaturated metal sites (CUS) to test different energetics, whereas non-CUS MOF atoms were assigned unmodified UFF parameters. Generic force fields such as UFF (Rappe et al., 1992) and Dreiding (Mayo et al., 1990) have been shown useful to simulate methane adsorption in MOFs (Düren et al., 2004; Wilmer et al., 2012; Barin et al., 2014; Gómez-Gualdrón et al., 2014a; Sezginel et al., 2015) and to reasonably rank MOFs based on methane adsorption (McDaniel et al., 2015). As shown by Rana et al. (2014), although UFF predicts slightly higher uptakes than Dreiding, UFF- and Dreiding-based methane isotherms are still relatively similar. Also, as shown in selected simulation/experiment comparisons in Figure S7, depending on the MOF, either force field can be the one that reproduces experimental data more accurately. Methane heats of adsorption reported for these systems were obtained directly from GCMC simulation using the fluctuation method (Nicholson and Parsonage, 1982):

$$\Delta H_{ads} = RT - \frac{\langle \mathcal{V} N \rangle - \langle \mathcal{V} \rangle \langle N \rangle}{\langle N^2 \rangle - \langle N \rangle^2} \qquad (1)$$

where the brackets denote ensemble averages, R is the ideal gas constant, T is the temperature, N is the number of adsorbate molecules in the system, and $\mathcal{V}$ is the potential energy of the system.

Quantum mechanics calculations for the "methane + substituted phenyl ring" complexes discussed in Section 3.5 were done using the Gaussian 09 software (Frisch et al., 2009). The structural optimizations of these complexes were based on the second order Møller-Plesset (Head-Gordon et al., 1988) level of theory, and we used the 6-311++G(d,p) (Clark et al., 1983; Frisch et al., 1984; Krishnan et al., 1980; McLean and Chandler, 1980) basis set for non-metal atoms and the LANL2DZ (Dunning Jr and Hay, 1977) basis set and respective effective core potentials (Hay and Wadt, 1985) for metal atoms. The self-consistent field convergence criterion was set to 10^{-8}. Binding energies were corrected for basis set superposition error using the method of Boys and Bernardi (1970). All optimized geometries for these complexes are shown in Tables S1-S3.

3. RESULTS AND DISCUSSION

For a material to have a high methane (volumetric) deliverable capacity, it needs to have a large number of adsorption sites per volume of material, M (Simon et al., 2014). For methane physisorption, these "sites" are not necessarily small, well defined regions due to the relatively weak adsorbate/adsorbent interactions. Traditionally, adsorption sites are thought of as located on the material (pore) surface, making the density of adsorption sites proportional to the volumetric surface area (Gómez-Gualdrón et al., 2014b; Martin and Haranczyk, 2013). Alternatively, it is possible to think of a *working* definition of an adsorption site as *any* location that can be occupied by a methane molecule. Thus, if a material has sufficiently large pores, methane molecules can occupy positions far from the pore surface, and thus some "sites" are not related to the volumetric surface area of the material but rather to the void fraction. Under this

definition, the density of adsorption sites is equivalent to the methane saturation loading (M) of the material (Simon et al., 2014).

At the storage and discharge pressures (P_H and P_L), different fractions (f_H and f_L) of these sites will be occupied. The deliverable capacity of a material is then $(f_H - f_L)M$. The difference $f_H - f_L$ is called the fractional deliverable capacity (FDC) (Gómez-Gualdrón et al., 2014b; Simon et al., 2014), and it depends on the energy of adsorption. Note that sites close to a pore wall provide higher adsorption energies than sites far from any pore wall. Creating walls, and thus sites of higher adsorption energies, requires sorbent atoms, which take up space and limit the saturation loading M. There is, thus, a "material penalty" to create strong adsorption sites. Evidently, the challenge in material design for gas storage applications is to maximize M, i.e. to reduce the material penalty, while simultaneously endowing the adsorption sites with optimal energetics so that FDC is maximized. With this in mind, let us now consider different adsorption scenarios to assess different combinations of M and adsorption energetics.

3.1. Scenario 1: Methane adsorption on FCC-arranged pockets

One scenario that can be conceived is a nanoporous material that provides tailored adsorption "pockets" for methane to sit, where each adsorption pocket is capable of hosting one and only one methane molecule, similar to methane molecules trapped in clathrate cages (Gómez Gualdrón and Balbuena, 2007; Sloan, 2003). The exact geometrical arrangement and identity of the atoms involved in the creation of these tailored sites determines both the energetics of the methane pockets and the material penalty to create them. The latter, in turn, determines the number of methane pockets per volume of material and thus the saturation loading M. As a reference, in the case of clathrate cages M is ~180 cc(STP)/cc (Sloan, 2003).

In a computational simplification of the above scenario, let us consider methane adsorption in a model representing regularly spatially distributed adsorption pockets, where each pocket is denoted by the position of its center and the number of pockets per volume is equivalent to M. In the simplified model, we define the distance between the centers of the pockets as the pocket-pocket distance d, and an increase in d effectively represents an increase in the material penalty. Since we seek to maximize M, we distribute the pockets in space using an FCC (**fcu**) arrangement, which yields the highest achievable M for a given d. Note, for instance, that the FCC arrangement for $d \sim 4.17$ Å (the equilibrium distance of the methane TraPPE model) reproduces the density of solid methane (~690 cc(STP)/cc) (Ramsey, 1963). Figure 2a shows a two-dimensional slice for such an arrangement. Figure 2b plots M versus d, with the inset displaying the rhombic-dodecahedral shape of the methane pocket that is being represented. Indeed, the simplified model represents a rhombic dodecahedral honeycomb (Figure S1).

To investigate the effect of energetics, let us endow the pockets with different energies U_o and simulate the respective methane deliverable capacity for different d values. Note that for each d value, we systematically explored different energetics of the pockets until we found the one to maximize the deliverable capacity. Figure 2c shows the maximum deliverable capacity for each d. If methane-methane interactions are neglected, the model is equivalent to the Langmuir adsorption model, and consistent with this model (Simon et al., 2014), the maximum FDC (for storage at 65 bar and delivery at 5.8 bar) is 0.52, obtained with different heats of adsorption depending on d. For the Langmuir model, the maximum deliverable capacity for a given M is simply $0.52M$ (indeed the bottom curve in Figure 2c is simply the curve in Figure 2b times 0.52), and the deliverable capacity reaches ~345 cc(STP)/cc for $d \sim 4.17$ Å (i.e. for M equal to the density of solid methane). On the other hand, if methane-methane interactions between methane

molecules in different pockets are considered—a mean interaction energy between two methane molecules in different pockets is considered depending on the distance between the center of the relevant pockets; details in Supplementary Section I—and the pockets are sufficiently close, the maximum FDC is higher than 0.52, and the maximum deliverable capacity is higher than 0.52 M as the top curve in Figure 2c shows for low *d* values. The reason is that methane-methane attractive interactions boost methane loading at the storage pressure while leaving the methane loading at the discharge pressure relatively unaffected. A similar mean field approximation of this model results in the Temkin adsorption model, which is a perturbation of the Langmuir model (Simon et al. 2014).

The top curve in Figure 2c shows that as *d* becomes smaller (i.e. the pocket centers come closer) the heat of adsorption needed to maximize the deliverable capacity (i.e. the optimal heat of adsorption) decreases, because the methane-methane attractive interactions compensate for the lower attraction provided by the pockets. From Figure 2c we see that the ARPA-E target is reached for d < 5.3 Å (i.e. M > 369 cc(STP)/cc (Figure 2b)) if methane-methane interactions are considered. Note that if methane-methane interactions are neglected, the ARPA-E target is reached only for d < 4.4 Å (i.e. M > 609 cc(STP)/cc (Figure 2b))—recall that 690 cc(STP)/cc is the density of solid methane.

With *d* ~5.3 Å the ARPA-E target is reached with an optimal heat of adsorption of 11.5 kJ/mol (Figure 2c), which yields an FDC of 0.85. Remarkably, as *d* decreases, FDC approaches *one*, and thus the deliverable capacity approaches *M*. So when the pocket-pocket distance *d* approaches d ~ 4.17 Å—and M approaches the density of solid methane—the maximum deliverable capacity approaches ~690 cc(STP)/cc! The simulations for scenario 1 show a beneficial effect of methane-methane interactions on methane deliverable capacity due to the (unrealistic)

confinement of methane molecules to well-defined pockets. It is apparent, however, that such low *d* or high *M* is impossible to obtain when actual atoms are involved in the creation of the pockets. Notably, relatively minor increases in *d* sharply decrease the maximum deliverable capacity. For instance, the maximum deliverable capacity is already at *50%* of the ARPA-E target for *d* values as low as 5.9 Å.

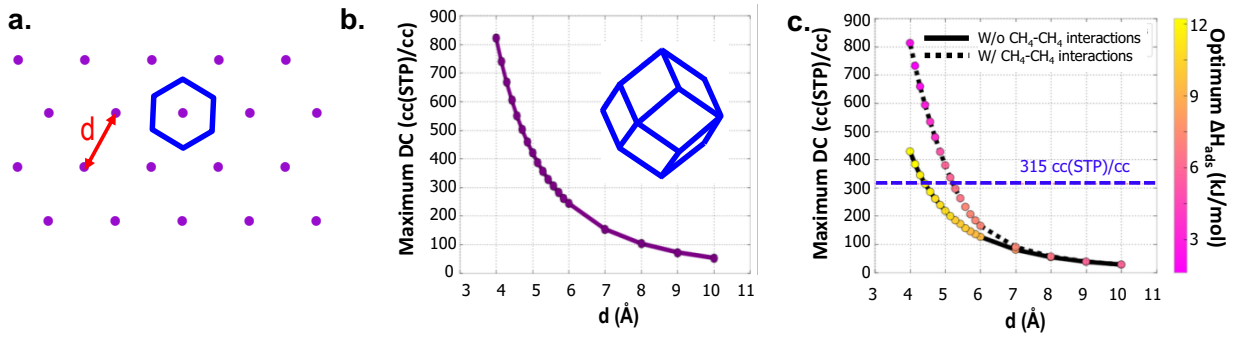

Figure 2. Methane adsorption in scenario 1. a) Two-dimensional slice of the FCC (**fcu**) arrangement of methane pockets (the purple dots represent the centers of the pockets), with *d* being the distance between the centers of adjacent pockets. A two dimensional slice of the contour of a methane pocket is also shown in blue. b) Density of sites or saturation loading, *M*, versus *d*. The inset shows the rhombic-dodecahedral shape of the contour of the methane pocket. c) Maximum deliverable capacity (DC) versus pocket-pocket distance *d* with (top curve) and without (bottom curve) methane-methane interactions. Points are colored according to the optimal heat of adsorption.

3.2. Scenario 2: methane adsorption onto a homogeneous interaction field.

Contrary to the well-defined adsorption sites that confine methane molecules in scenario 1, the pores of a typical adsorbent material with non-commensurate adsorption provide freedom for methane molecules to spatially organize themselves during adsorption. For instance, in highly porous materials (which also yield the highest M values), adsorbed methane molecules loosely sit in the interaction field created by the pore atoms. Thus, for scenario 2 let us consider methane adsorption onto an artificially created homogeneous interaction field as a simplified limiting case corresponding to *no material penalty*. Analogous to scenario 1, let us endow the field with tunable adsorption energetics. Here we always consider methane-methane interactions to avoid

unrealistic overlap of methane molecules. The overlap is prevented by the repulsive part of the methane-methane interaction potential. See further details on the simulation algorithm used for scenario 2 in the Supplementary Section I.

Figure 3a shows the adsorption isotherms for different background fields corresponding to different heats of adsorption. For comparison, the black dashed isotherm shows the variation of the density of bulk methane gas with pressure, which effectively corresponds to the case with an interaction field featuring a 0 kJ/mol energy of adsorption. Figure 3b shows the deliverable capacities for different heats of adsorption calculated from the isotherms in Figure 3a. In this scenario, deliverable capacities equal to or higher than the ARPA-E target (315 cc(STP)/cc) were obtained with heats of adsorption in the ~6.7 - 10.1 kJ/mol interval. The highest deliverable capacity was 357 cc(STP)/cc for a heat of adsorption of 8.6 kJ/mol.

Remarkably, the optimal heats of adsorption that lead to deliverable capacities surpassing the ARPA-E target are not extraordinarily high and are similar to those observed in highly porous materials synthesized and tested to date (Mason et al., 2014; Peng et al., 2013). Note, however, that the reported heats of adsorption do not reflect the heterogeneity of adsorption sites in synthesized materials. For instance, locations close to the pore walls have high heats of adsorption, but at other locations such as at the centers of pores, the associated heats of adsorption are much lower. Indeed, the question and associated challenge that derives from this scenario is whether it is possible to synthesize a highly porous material (i.e. low material penalty and thus high M) that can provide a *homogeneous* interaction field with such an optimal heat of adsorption.

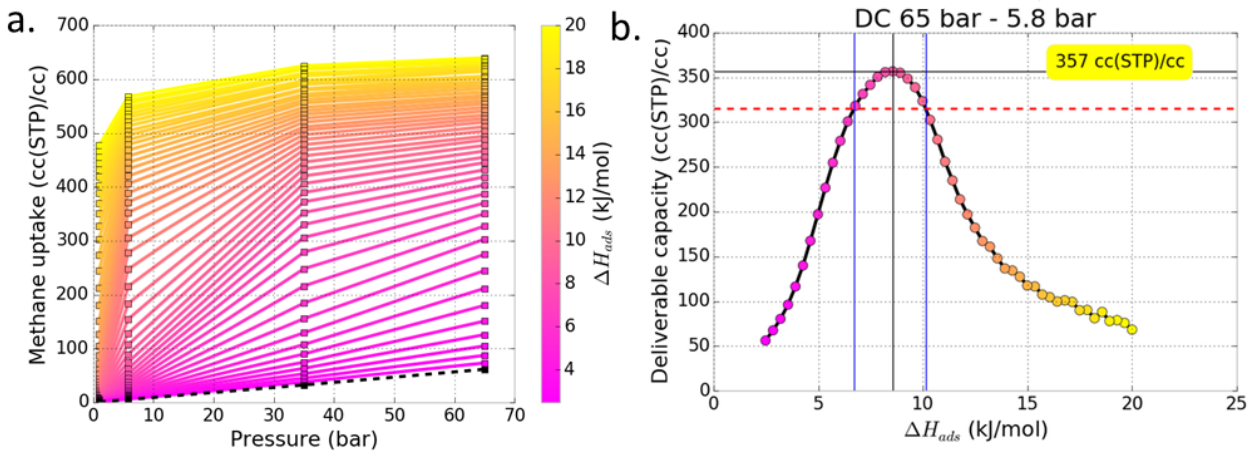

Figure 3. Methane adsorption in scenario 2. a) Methane adsorption isotherms in a background interaction field. The heat of adsorption associated with the field for each isotherm is denoted by the color of the isotherm according to the vertical color bar. The black dash-line isotherm corresponds to the bulk density of methane at different pressures. b) Deliverable capacities extracted from panel *a* for different heats of adsorption associated with the background field. Points above the horizontal dashed line exceed the ARPA-E target. The color of the points corresponds with the heat of adsorption in (a).

3.3. Scenario 3: Methane adsorption around discrete pseudoatoms

To increase the realistic character of the adsorbent, let us now consider a scenario where an inherently *heterogeneous* interaction field is created by the LJ potential of discrete pseudoatoms regularly distributed in space. In this case, the material penalty is significantly lower (high *M*) than in most existing materials. The exact value depends on the spatial distribution and σ parameter, representing the size, of the pseudoatoms. The spatial distribution of the pseudo-atoms and the LJ ε and σ parameters together determine the characteristic adsorption energetic landscape. Here we assign the pseudoatoms the σ parameter that gives them the size of a carbon atom (σ_c = 3.43 Å). We modify the ε parameter of the pseudoatoms as multiples of the original ε parameter of a carbon atom (ε_c = 52.8 K).

We explored four different spatial distributions for the pseudoatoms corresponding to the arrangements illustrated in Figure 4a: simple cubic (SC or **pcu**), body-centered cubic (BCC or **bcu**), face-centered cubic (FCC or **fcu**), and diamond (**dia**). We varied the carbon-carbon

distances *CC* between pseudoatoms by increments of 0.4 Å by modifying the unit cell lattice constant *a* accordingly. The smallest values of *CC* create a scenario somewhat similar to scenario 1. Consider for instance the **pcu** case for $CC \leq 5.2$ Å: the pseudoatoms at the vertices of the cubic units create a pocket at the center of the unit cell that can accommodate only one methane molecule. The largest values of *CC*, on the other hand, create a scenario similar to scenario 2 in that the material penalty approaches zero and adsorption sites are not well defined. The difference is that the created interaction field is heterogeneous instead of homogeneous.

Figure 4b summarizes the results for the **pcu** spatial arrangement (see other cases in SI). Since the behavior is slightly different below and above $a = CC = 5.2$ Å, let us start by discussing $a \leq 5.2$ Å. As mentioned above, for these *a* values, the systems have one pocket per unit cell. At 65 bar, these pockets are completely filled with methane (one methane molecule each) if the interaction is strong enough (epsilon multiplier ≥ 8), so the methane loading is equal to *M*. Since *M* rapidly decreases from 430 cc(STP)/cc to 265 cc(STP)/cc when *a* changes from 4.4 to 5.2 Å, the methane loading decreases as well. We found that in this *a* range, the *FDC* is relatively high if the heat of adsorption is optimal. This is somewhat similar to scenario 1 where, provided the heat of adsorption was optimal, *FDC* was close to 1.0 when *d* was close to 4.17 Å. This makes the deliverable capacity very sensitive to *M*. Here the highest deliverable capacity (370 cc(STP)/cc) was obtained when *M* was the highest (430 cc(STP)/cc for $a = 4.4$ Å) and the heat of adsorption was ~17 kJ/mol (epsilon multiplier equal to eight). Related to the impact of material penalties, the **pcu** arrangement produced pockets with the highest *M* among the four spatial arrangements studied in this subsection. Yet, this highest *M* was only ~60% of the highest *M* explored in scenario 1 (~690 cc(STP)/cc).

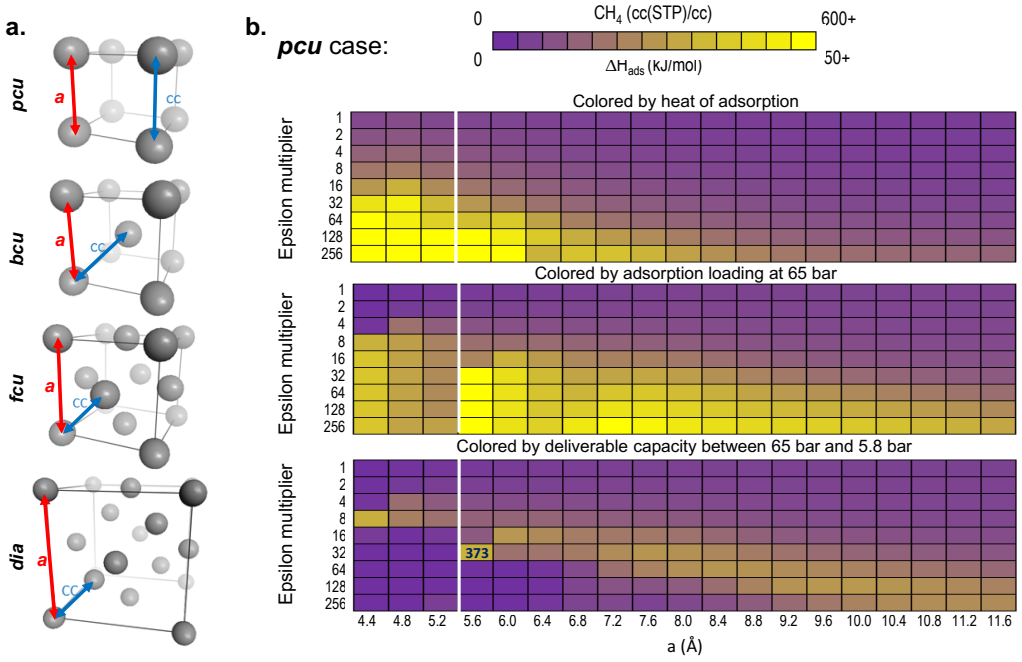

Figure 4. Methane adsorption in scenario 3. a) The four different pseudoatom arrangements (**pcu**, **bcu**, **fcu**, and **dia**) explored in scenario 3. For the four cases, the lattice constant *a* was varied using a 0.4 Å step. b) Data for the **pcu** case. In all panels, each pixel corresponds to a combination of ε multiplier and lattice constant *a*. The color of the pixel indicates either methane heat of adsorption (top panel), methane loading at 65 bar (middle panel), or methane deliverable capacity between 65 and 5.8 bar (bottom panel) according to the top colored scale bar. The ε multiplier is in reference to that of carbon (ε_c= 52.8 K). The combination yielding the highest deliverable capacity (373 cc(STP)/cc) is annotated in the corresponding pixel.

Now let us consider $a > 5.2$ Å when the methane pockets vanish and the methane adsorption sites become less defined. In this range the relation between methane loadings at 65 bar and the heats of adsorption is relatively straightforward: they both increase with the epsilon multiplier for a fixed *a*, and they both decrease with *a* for a fixed epsilon multiplier. Note that without epsilon multipliers the heats of adsorption and the methane adsorption loadings were never higher than ~7 kJ/mol and ~60 cc(STP)/cc, respectively. However, upon applying the epsilon multipliers, the loadings at 65 bar tended to be higher than when $a \leq 5.2$ Å (due to lower material penalty), although the *FDCs* tended to be lower. Indeed, the highest deliverable capacity (373 cc(STP)/cc) for $a > 5.2$ Å was only slightly higher than the highest for $a \leq 5.2$ Å although with a higher loading at 65 bar (613 cc(STP)/cc) and lower *FDC* (0.54). This occurred for $a = 5.6$ Å

and epsilon multiplier equal to 32, which corresponded to a heat of adsorption of ~24.9 kJ/mol. The highest deliverable capacity for the **pcu** and other spatial arrangements and the corresponding parameters are summarized in Table 1.

Table 1. Highest deliverable capacity (DC) between 65 and 5.8 bar obtained for the four different types of pseudoatom arrangements (**pcu**, **bcu**, **fcu**, and **dia**) explored in scenario 3, and the properties corresponding to each highest deliverable capacity value.

Pseudoatom Arrangement	**Highest DC cc(STP)/cc**	**Properties corresponding to highest DC**			
		d (Å)	ε multiplier	ΔH_{ads} (kJ/mol)	CH_4 @ 65 bar (cc(STP)/g)
pcu	373	5.6	32	24.9	613
bcu	326	12.0	128	10.8	401
fcu	333	6.8	16	19.4	398
dia	302	16.6	64	11.9	322

As with the optimal heats of adsorption for scenarios 1 and 2, notice that the optimal heats of adsorption listed in Table 1 are within the range of heats of adsorption reported for synthesized and tested materials. Here, however, these heats of adsorption are provided by a remarkably small amount of material. As a reference, consider that with an epsilon multiplier of 256 the volume occupied by a pseudoatom provides an amount of dispersion interactions around sixteen times higher than that provided when a regular carbon atom occupies said volume. Thus the results here quantify potential benefits if new types of binding sites that are small in volume but that strongly polarize methane were to be incorporated in adsorbent materials. This suggestion has also been put forward by Mason *et al*. (2014), although the question remains whether synthesizing sites with those characteristics is possible.

3.4. Scenario 4: Methane adsorption in pseudoatom-thick networks

Different from the isolated pseudoatoms studied in scenario 3, the constituents of actual porous materials are interconnected. So let us increase the realistic character of the adsorbent once

again, by considering the eight systems shown in Figure 5a. These systems are pseudoatom-based networks based on the **pcu**, **bcu**, **fcu**, and **dia** topologies. These networks effectively represent the limiting cases of the thinnest networks one could get: each node is constituted by a single pseudoatom, and the connections between nodes are one pseudoatom in thickness. Connected pseudoatoms (σ = 3.43 Å) in the illustrated systems are separated by 4.1 Å, which prevents the accommodation of methane molecules (σ_{CH4} = 3.73 Å) between them. The ε parameters of the pseudoatoms are modified similarly to scenario 3: by multiplying the original epsilon (52.8 K) by factors of 1, 2, 4, 8, 16, 32, 64, 128, and 256, respectively.

The **pcu-1**, **bcu-1**, **fcu-1**, and **dia-1** networks have the same distance between nodes; so do the **pcu-2**, **bcu-2**, **fcu-2** and **dia-2** networks. Figure 5b summarizes the findings for methane adsorption in these thin networks. For a given type of network, the heat of adsorption increases with the epsilon multiplier and decreases when the net is expanded. For networks with the same distance between nodes, the heat of adsorption typically follows the trend **fcu** > **bcu** > **pcu** > **dia**. This trend can be explained by the number of pseudoatoms per volume, which also follow this order. The methane loadings at 65 bar increase with the epsilon multiplier, unless the saturation loading *M* is already reached. We obtained high methane loadings at 65 bar in these systems depending on the epsilon multiplier and the density and topology of the network. The shortest networks of **pcu** and **dia** topology, **pcu-1 and dia-1**, reached methane loadings higher than 315 cc(STP)/cc with a relatively low epsilon multiplier of 32. So did the longest networks of **bcu** and **fcu** topology, **bcu-2** and **fcu-2**. Note that methane loadings in **bcu-1** and **fcu-1** (263 cc(STP)/cc and 95 cc(STP)/cc, respectively) are limited by material penalties. Indeed, the values of *M* for these two networks are 263 and 95 cc(STP)/cc, respectively.

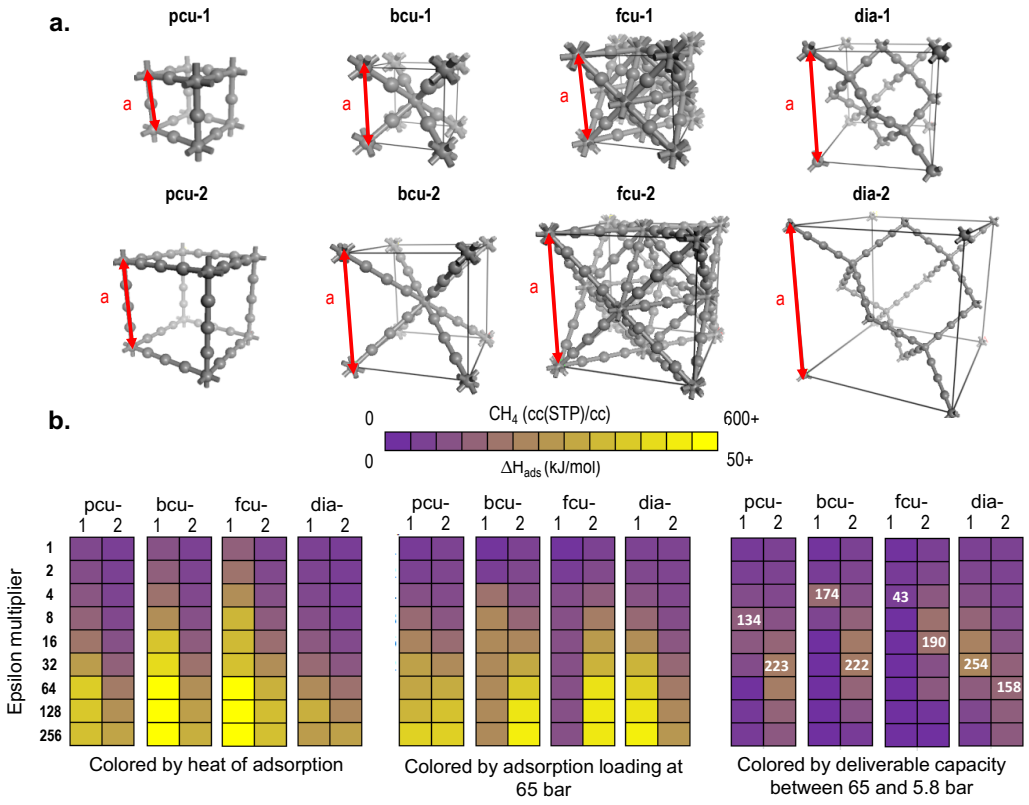

Figure 5. Methane adsorption in scenario 4. a) Structures of the pseudoatom-thick networks investigated in scenario 4. In the networks, all neighboring atoms are separated by a distance of 4.1 Å. b) Data for the structures shown in panel a). In all panels, each pixel corresponds to a combination of epsilon multiplier and network. The color of the pixel indicates either methane heat of adsorption (left panel), methane loading at 65 bar (middle panel), or methane deliverable capacity between 65 and 5.8 bar (right panel) according to colored scale bar. The epsilon multiplier is in reference to the epsilon of carbon (ε_c= 52.8 K). The highest deliverable capacity for each network is annotated in the corresponding pixel.

The highest deliverable capacities for the systems studied in this subsection were obtained for **pcu-2 (**223 cc(STP)/cc**)**, **bcu-2 (**222 cc(STP)/cc**)** and **dia-1 (**254 cc(STP)/cc**)** with moderate heats of adsorption (~18, ~16 and ~14 kJ/mol, respectively). Note that contrary to the previously investigated scenarios, *as somewhat more realistic material penalties come into play, none of the calculated deliverable capacities are higher than the ARPA-E target.* The best value corresponds to ~80% of the target, although it is ~30% higher than the current best deliverable capacities for current materials. Note the recurring theme in the four scenarios investigated to this point: high deliverable capacities depend on whether it is feasible to use small-volume

chemical sites that both keep the material penalty low (high *M*) and provide heats of adsorption in the ~10 - 25 kJ/mol range (high *FDC*).

3.5 Scenario 5: Methane adsorption in MOF systems with localized strong binding sites

Based on the results for scenarios 1 through 3, it seems that there is not a fundamental thermodynamic limit that forbids obtaining methane deliverable capacities surpassing the ARPA-E target. However, as already apparent in scenario 4, the material architectures and chemical characteristics needed to reach the desired deliverable capacity of 315 cc(STP)/cc between 65 and 5.8 bar may be impossible to achieve. Indeed, one material design requirement is to have small-volume sites that also provide strong binding for methane without much help of confinement effects. However, we show below that, from a chemical point of view, methane is somewhat insensitive to the type of chemical moieties it interacts with.

Figure 6a shows the binding energies from quantum mechanics (MP2) calculations for methane with phenyl rings mono-substituted with different chemical groups. When methane binds or adsorbs on top of the ring, the binding energy ranges between ~3 and ~5 kJ/mol for the different substitutions, only moderately improving (in absolute terms) the "on-top" binding energy of the non-substituted ring ("H" in Figure 6a). Among "side-binding" configurations, the strongest methane binding energy was interacting with hydroxyl groups, but it was only ~3 kJ/mol. These low binding energies suggest that modification of methane adsorption properties by incorporation of organic chemical substituents in existing materials are mainly due to changes in material textural properties such as surface area and pore size (where pore size in turn impacts the heat of adsorption through confinement effects).

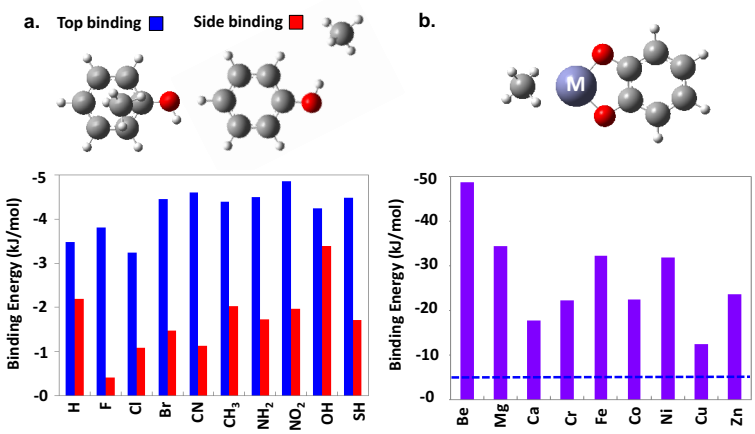

Figure 6. Methane binding energies to different chemical moieties estimated from quantum calculations. a) Binding of methane to a phenyl ring mono-substituted with different functional groups. Typically, two minima were identified: one with methane binding on top of the ring (blue bars), and another with methane side binding to the functional group (red bars). b) Binding of methane to a catechol metalated with different divalent metal atoms (atomic number increases from left to right). Horizontal dashed line refers to the highest binding energy in panel a. (grey atoms: C, red atoms: O, white atoms: H, purple atoms: metal).

A chemical moiety that could be an exception is a coordinatively unsaturated metal site (CUS). These sites have been shown to interact strongly with methane (Chen et al., 2011; Wu et al., 2009). However, in MOFs, these sites normally belong to the inorganic nodes. Therefore, increasing the number density of CUS would normally imply increasing the number of inorganic nodes per unit cell volume, which would lead to denser networks and highly detrimental material penalties. An alternative strategy for incorporating CUS into materials such as MOFs is then using organic linkers, for example metalated catechol groups. These types of groups have been successfully incorporated into porous materials using different synthesis strategies (Fei et al., 2014; Tanabe et al., 2010; Weston et al., 2012), and they have been studied theoretically as well (Colón et al., 2014; Getman et al., 2011; Raksakoon et al., 2015).

Figure 6b shows the binding energy for the side-binding of methane to the CUS of a few metalated catechols. The typically adopted geometry is illustrated at the top of Figure 6b. Notice that there is a rather large variability of the binding energy (~12 - 48 kJ/mol) depending on the

type of metal used, which in principle would enable the tuning of the interactions of methane with the organic linker. On these grounds, let us now consider how different energetics and spatial distributions of CUS introduced to existing MOF platforms via metalated catechol groups affect methane loadings and methane deliverable capacity.

The selected MOF topologies are schematized in Figure 7 (top row) where examples of CUS locations are shown by pink and blue spheres. The **csq** topology corresponds to the MOF **NU-1000** (Mondloch et al., 2013), for which non-backbone metalated catechol ligands (Figure 7 left-bottom) can be attached to the inorganic node via solvent-assisted ligand incorporation (SALI) (Deria et al., 2013). The **pcu** topology corresponds to zinc-based MOFs **IRMOF-1**, **IRMOF-10**, and **IRMOF-16**, and the **fcu** topology corresponds to the zirconium-based MOFs **UiO-66**, **UiO-67**, **NU-800**, and **UiO-68**. For these two topologies, "node-connecting" (backbone) metalated catechol-based linkers (Figure 7 right-bottom) analogous to those of the parent MOFs can be incorporated through strategies such as solvent-assisted linker exchange (SALE) (Karagiaridi et al., 2014).

Topology, linker length, and the number and position of metalated catechols in the linker all affect the spatial distribution and number density of CUS. Note that interactions between methane and CUS are stronger than those obtained with standard UFF σ and ε parameters for metal atoms. CUS are often discussed as playing an important role in methane adsorption (Karra and Walton, 2008; Uzun and Keskin, 2015; Wu et al., 2015). Indeed, it is not uncommon to find significant disagreement between experimental and UFF-based simulated methane isotherms in MOFs with a high volumetric density of CUS. For instance, UFF-based simulations somewhat underestimate experimental high-pressure methane uptakes in HKUST-1 (Koh et al., 2015). Koh et al. (2015) derived CH_4-CUS interaction parameters from *ab-initio* calculations, which were

used to obtain simulated isotherms reproducing experimental data for HKUST-1. In this section we do not aim to model a CH_4-CUS interactions for a particular metal, but rather we aim to thoroughly explore a wide range of hypothetical CH_4-CUS interactions. Thus, to rapidly examine different CUS energetics, let us treat the metal atoms of the linkers as pseudoatoms with LJ parameters σ_{CUS} = 2.46 Å (the UFF σ parameter for zinc) and tunable ε_{CUS} (as multiples of the UFF ε parameter for zinc, ε_{Zn} = 62.4 K).

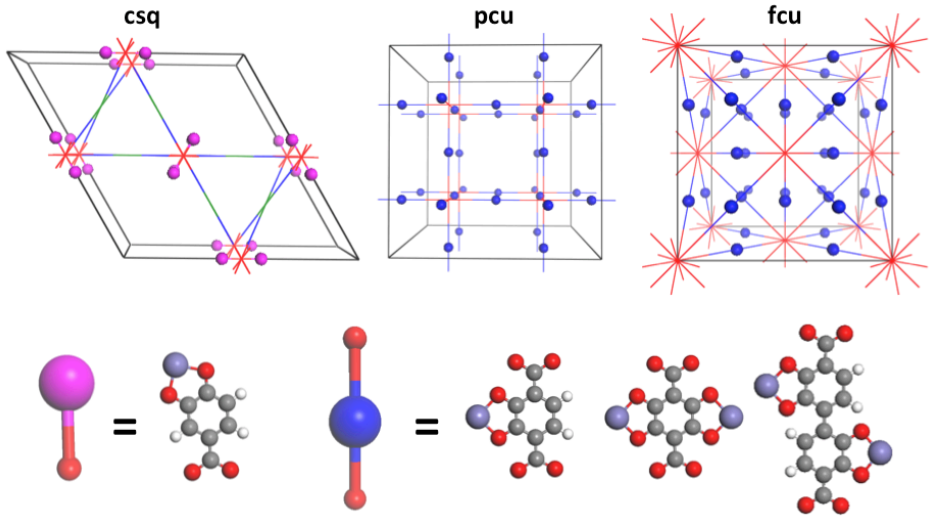

Figure 7. Introduction of coordinatively unsaturated sites (CUS) to MOFs. Metalated catechol groups were introduced to MOFs based on the three topologies illustrated in the top row: **csq** (NU-1000), **pcu** (IRMOF-1, IRMOF-10, IRMOF-16), and **fcu** (UiO-66, UiO-67, NU-800, UiO-68). The CUS spatial distribution in each topology is schematized by the positions of pink and blue spheres in the networks illustrated in the top row. Examples of the exact chemical moieties introduced in the above-mentioned MOFs are illustrated in the bottom row. (carbon: gray; oxygen: red; hydrogen: white; metal: purple). Additional functionalized linkers are shown in Figure S6.

Figures 8 (**csq**), 9 (**fcu**), and 10 (**pcu**) summarize the resulting methane loadings and deliverable capacities for different CUS incorporation schemes and ε_{CUS} values. Note that the achieved number density of CUS is relatively low (4.5 CUS/nm^3) for the CUS incorporation in **NU-1000** (Figure 8). However as the epsilon multiplier for the CUS increases up to 250, the methane loading rapidly increases with respect to the parent MOF from ~180 to ~250

cc(STP)/cc. Further increases in the epsilon multiplier increase the methane loading more slowly. On the other hand, the deliverable capacity only increases up to 170 cc(STP)/cc with epsilon multiplier increases up to 100. This is a 40 cc(STP)/cc improvement over the deliverable capacity of the parent **NU-1000**. To estimate *M* for the parent MOF and its derivatives, let us use the geometric void fractions of these materials and the density of liquid methane (590 cc(STP)/cc), such that *M* is equal to "V_f x ρ_{CH4}". With this approximation, we estimate *M* = 470 cc(STP)/cc and *FDC*= 0.29 for the parent **NU-1000** and *M* = 450 cc(STP)/cc and *FDC*=0.38 for the derivative of **NU-1000** having the optimal epsilon multiplier. However, while we were able to improve the performance of the parent **NU-1000**, we did not obtain deliverable capacities surpassing the highest simulated deliverable capacity reported in Figure 1.

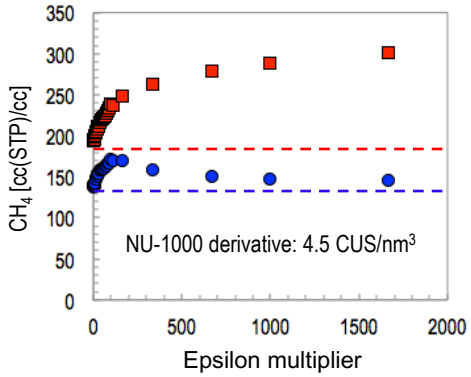

Figure 8. Methane adsorption in metalated NU-1000. Methane loading at 65 bar (red squares) and deliverable capacity between 65 and 5.8 bar (blue circles) versus epsilon multiplier for the metal CUS for the NU-1000 derivative. The red and blue horizontal lines correspond to the methane loading and deliverable capacity of the parent MOF NU-1000.

Let us now consider derivatives of parent **fcu** and **pcu** MOFs. We should note that for a given linker or parent **fcu** or **pcu** MOF, there are different ways to incorporate CUS that lead to the same number density of CUS in the derivative structures. In general, arrangements corresponding to the same number density of CUS produced similar methane loading (and

deliverable capacity) versus epsilon multiplier curves, so we only plotted selected curves in Figure 9 and Figure 10 for the sake of clarity.

Figure 9 shows results based on the parent **fcu** MOFs **UiO-67**, **NU-800**, and **UiO-68**. As with the derivatives of **NU-1000**, the incorporation of CUS in parent **fcu** MOFs leads to notable improvements in the methane loadings at 65 bar. However, despite this improvement in loadings, an inspection of Figure 9 (bottom row) clearly shows that for this highly dense topology, the incorporation of CUS was detrimental to the deliverable capacity of the parent MOFs. Even in the best derivative case, which was a derivative of **NU-800**, the optimal epsilon multiplier only led to a simulated deliverable capacity matching the parent MOF **NU-800**, which without any modification is already among the best performer MOFs (Gómez-Gualdrón et al., 2014a; Zhang et al., 2015).

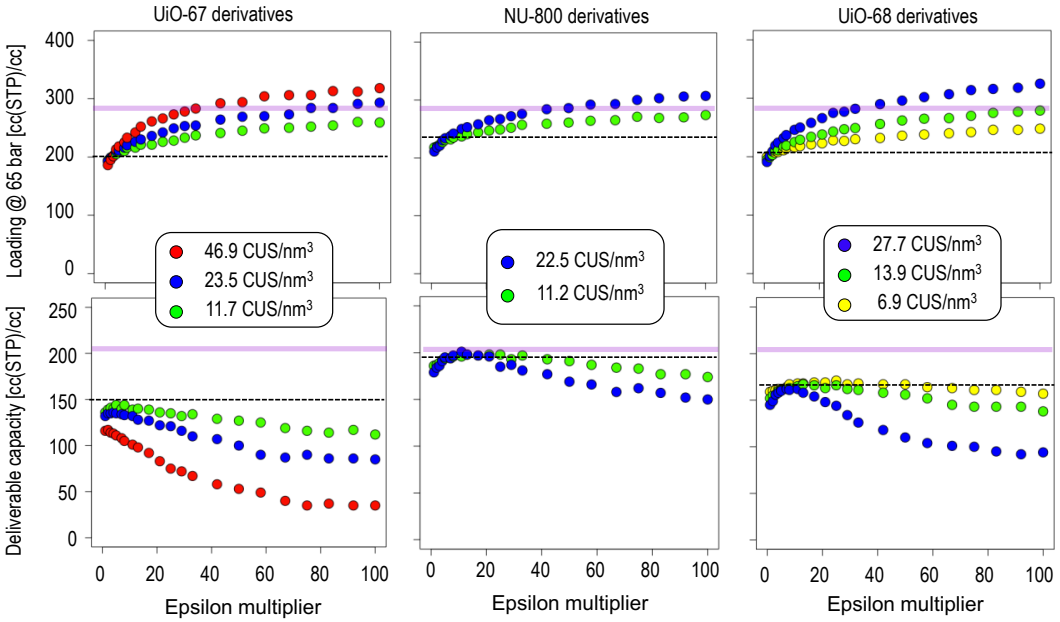

Figure 9. Methane adsorption in metalated fcu MOFs. Methane loading at 65 bar (top row) and deliverable capacity between 65 and 5.8 bar (bottom row) versus the epsilon multiplier for the metal CUS for different derivatives of parent **fcu** MOFs. The inset box relates the color of each curve and the respective CUS number density. The dashed lines represent the methane loading (top row) or deliverable capacity (bottom row) of the parent MOF. Solid lines represent the highest value of methane loading (top row) or deliverable capacity (bottom row) among the MOFs in Figure 1.

Figure 10 (top row) summarizes the relationships between methane loading and epsilon multipliers obtained for CUS incorporation in **pcu** MOFs (**IRMOF-1**, **IRMOF-10**, and **IRMOF-16**). Once again, CUS incorporation leads to significantly higher loadings than in the parent MOF. When considering the deliverable capacity (Figure 10 bottom row), no combination of CUS incorporation scheme and epsilon multiplier leads to an improvement of the deliverable capacity of the parent **IRMOF-1**. However, most CUS incorporation schemes lead to improvement of the deliverable capacity of the less dense parent MOFs **IRMOF-10** and **IRMOF-16**. Remarkably, *the deliverable capacity of the functionalized **IRMOF-10** at the optimal epsilon value (217 cc(STP)/cc) is an improvement over the highest simulated deliverable capacity for any MOF* (Figure 1) albeit still far from the ARPA-E target. This occurred for CUS epsilon values ε_{CUS} around 60 times higher than the UFF epsilon of zinc ε_{Zn} = 62.4 K, which, translates into a binding energy of ~8 kJ/mol (in a "side-binding" configuration). Thus the desired methane-CUS interaction is moderate and somewhat lower than that of copper (~12 kJ/mol) in Figure 6b.

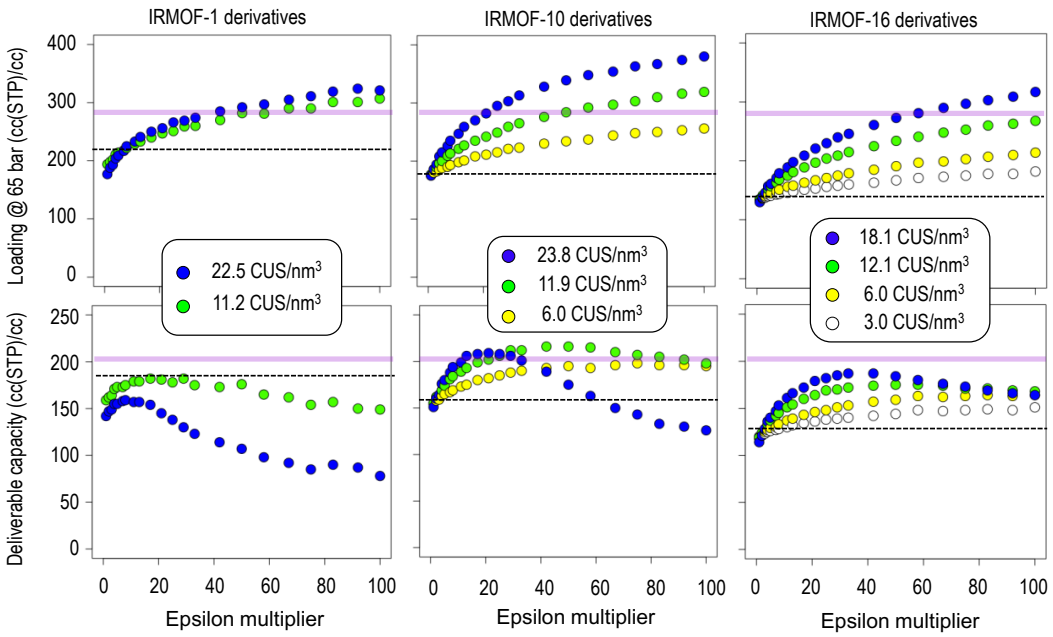

Figure 10. Methane adsorption in metalated pcu MOFs. Methane loading at 65 bar (top row) and deliverable capacity between 65 and 5.8 bar (bottom row) versus the epsilon multiplier for the metal CUS for different derivatives of parent **pcu** MOFs. The inset box relates the color of each curve and the respective CUS number density. The dashed lines represent the methane loading (top row) or deliverable capacity (bottom row) of the parent MOF. Solid lines represent the highest value of methane loading (top row) or deliverable capacity (bottom row) among the MOFs in Figure 1.

The structure corresponding to the best CUS incorporation scheme is shown in Figure 11, which also shows a summary plot relating the deliverable capacity to the heat of adsorption for all the combinations of CUS incorporation schemes and epsilon investigated in this subsection. Each point corresponds to a combination, with the color indicating the corresponding density of adsorption sites *M* or alternatively the void fraction. Since the void fractions calculated geometrically are independent of epsilon and different between the different MOFs investigated in this subsection, tracing the points with the same color in Figure 11 can be used to track the behavior of a given MOF. Recall that a higher heat of adsorption for a given MOF reflects the fact that the epsilon multiplier is higher.

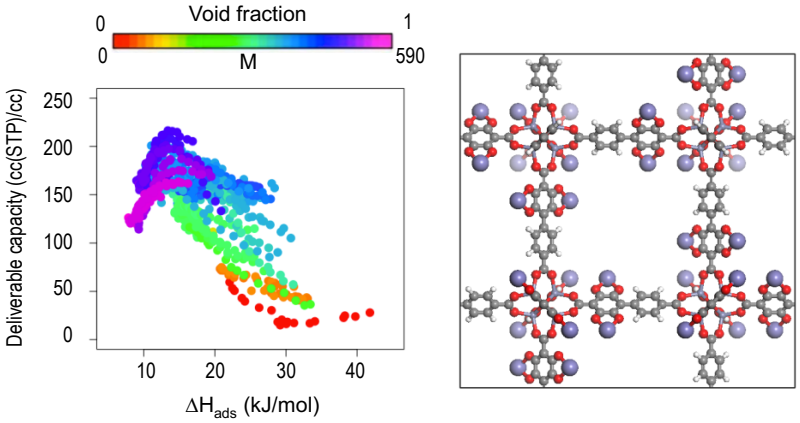

Figure 11. Methane adsorption in scenario 5. Left panel: Deliverable capacity for all MOFs for which CUS were introduced via metalated catechol groups versus heat of adsorption. Each point corresponds to a MOF, with the color indicating the void fraction of the structure according to the color scale at the top. Right panel: The structure of the MOF that resulted in the highest deliverable capacity. This structure is an IRMOF-10 derivative (oxygen, red; carbon; gray; zinc, small purple; CUS, big purple).

Note that for structures with low (high) *M,* the deliverable capacity has a downward (upward) trend as the heat of adsorption (i.e. CUS epsilon) increases. This is because the heat of

adsorption in structures with low M is already above the optimal value (the structure is highly dense and there are a large number of atoms to provide interactions with methane molecules). On the other hand, the heat of adsorption in unfunctionalized structures with high M is far below the optimal value (the structure is very low in density and there are only few atoms to provide interactions). However, we can see that for structures with moderately high *M*, the tuning of the epsilon multiplier of the CUS allows them to pass through their optimal heat of adsorption. Among the structures that pass through their optimal heat of adsorption, those with lower *M* produced higher deliverable capacities. This likely occurs because of the spatial heterogeneity of the energy field: in structures with higher *M* (i.e. higher void fraction), the heat of adsorption does not accurately reflect the energetics of adsorption far from the pore walls. Interestingly, independent of the artificial tuning of CUS epsilon parameters, the best materials screened in this subsection have saturation loadings *M* around 500 cc(STP)/cc (i.e. void fraction around 0.85), similar to results in previous reports (Chung et al., 2014; Gómez-Gualdrón et al., 2014b). Figure S9 shows results similar to Figure 11 but with different delivery temperatures (Gómez-Gualdron et al., 2014b). With delivery temperatures of 348 K and 398 K, the highest deliverable capacities were obtained with heats of adsorption around 10 kJ/mol higher than with a delivery temperature of 298 K. The best case with a delivery temperature of 398 K corresponded to a deliverable capacity of 266 cc(STP)/cc.

3.6. On methane adsorption in flexible MOFs

It should be mentioned that an intriguing alternative to achieve higher deliverable capacities in gas storage applications is the utilization of flexible MOFs, which can exhibit "S-shaped" adsorption isotherms in connection with adsorbate pressure-induced MOF structural transformation and/or MOF "gate-opening" behavior (Coudert et al., 2013; Schneemann et al.,

2014). If the MOF flexible structure is designed so the gate-opening occurs at a pressure P_G between P_H and P_L, a larger percentage of the gas stored at P_H could be expelled when the tank pressure falls to P_L than if the MOF is rigid. For instance, Deria *et al.* (2015) recently reported a ~15% boost in the propane deliverable capacity of a water-stable zirconium-based MOF (**NU-1105**) due to propane pressure-induced gate opening facilitated by linker flexibility. Specific to methane, Mason *et al.* (2015) recently reported sharply S-shaped methane isotherms for cobalt- and iron-based MOFs (Co(bdp) and Fe(bdp)), where most of the methane stored at 65 bar was released at 5.8 bar, resulting in deliverable capacities approaching 200 cc(STP)/cc. Indeed, the best scenario is one where all the methane stored at 65 bar is "deliverable," and thus the maximum methane uptake achievable at 65 bar represents an upper limit for the methane deliverable capacity of flexible MOFs. As a reference, for instance, Gomez-Gualdron *et al.* (2014b) reported a maximum methane uptake at 65 bar of ~290 cc(STP)/cc among ~48,000 MOFs. Here, CUS incorporation into IRMOF-10 is predicted to yield an uptake at 65 bar of 390 cc(STP)/cc (for a 100 epsilon multiplier; Figure 10). However, for the rigid structure the deliverable capacity was only ~125 cc(STP)/cc. Therefore, the challenge is to demonstrate whether it is possible to design MOFs that present both structural flexibility and high density of CUS that can interact strongly with methane.

4. SUMMARY AND CONCLUSIONS

After investigating five adsorption scenarios with different spatial distributions and energetics of adsorption sites, we conclude that *there is no apparent thermodynamic limit preventing a methane deliverable capacity between 65 and 5.8 bar equal to or higher than the 315 cc(STP)/cc ARPA-E target*. Scenario 1, which indirectly modeled adsorption in confined pockets, yielded a maximum deliverable capacity of 690 cc(STP)/cc (i.e. the density of solid methane!). However,

the necessary center-to-center distance between adjacent pockets *d* is equal to the size of methane (~4.2 Å) and is thus impossible to achieve. The maximum deliverable capacity sharply decreases as *d* increases, and it is already below the ARPA-E target for *d* values as low as 5.2 Å. Scenarios 2 and 3, in which we explored methane adsorption in an interaction field without material penalty (scenario 2) or with minimal material penalty (scenario 3), yielded maximum deliverable capacities around 370 cc(STP)/cc. It is noteworthy that the heats of adsorption leading to high deliverable capacities are in the range of methane heats of adsorption reported for materials synthesized to date. This showed the potential benefits of discovering chemical moieties that are small but provide a strong interaction field for methane, although the actual existence of such chemistry seems unlikely. Indeed, it became evident that *the limits that prevent meeting the ARPA-E deliverable capacity target arise from limitations in the chemistry and architecture of porous materials that can be realistically conceived*. This became evident in scenario 4 where upon tuning methane heats of adsorption in the thinnest networks that can be conceived, the maximum deliverable capacity was already ~255 cc(STP)/cc, corresponding to only ~80% of the ARPA-E target. While at this point it was clear that the ARPA-E target is virtually unattainable, in scenario 5 we explored more realistic designs of strong binding sites, seeking any potential improvements over the current highest deliverable capacities in the literature (~200 cc(STP)/cc). We incorporated coordinatively unsaturated sites (CUS) in parent MOFs and artificially tuned the CUS-methane interactions to optimize the deliverable capacity. Incorporation of CUS in the parent MOF **IRMOF-10** led to a deliverable capacity 217 cc(STP)/cc when the CUS-methane interactions somewhat resemble those of methane with coordinatively unsaturated copper sites. This material has a 0.85 void fraction and a ~15 kJ/mol heat of adsorption. Based on these findings, *the current apparent limits of deliverable capacity*

may be moderately surpassed by increasing the number density of CUS in a material while maintaining the void fraction relatively high. However, a significant increase in deliverable capacity must rely on changing the currently proposed operation conditions for ANG. It should also be noted that current deliverable capacities may still be practical for short-range commuter vehicles and recreational vehicles.

ASSOCIATED CONTENT

Supporting information: Additional simulation details for scenario 1 and 2. Results for other topologies in scenario 3. Results for UiO-66 derivatives in scenario 5. Linker structures used for making derivatives of **fcu** and **pcu** parent MOFs. Optimized geometries of "methane + functionalized phenyl ring" complexes. Excel file with tabulated data for screening in scenario 5. This material is available free of charge via the Internet at http://pubs.acs.org.

AUTHOR INFORMATION

Corresponding Author

E-mail: snurr@northwestern.edu

ACKNOWLEDGEMENTS

This research was supported by the U.S. Department of Energy, Office of Basic Energy Sciences, Division of Chemical Sciences, Geosciences and Biosciences, under Award DE-FG02-12ER16362. The computations were made possible by the high performance computing system QUEST at Northwestern University and the NERSC computing resources of the U.S. Department of Energy.

REFERENCES

Accelrys Software Inc., 2001-2011. Materials Studio. Accelrys Software Inc., San Diego, CA 92121, USA.

Allen, M.P., Tildesley, D.J., 1990. Computer Simulation of Liquids. Oxford University Press, Oxford.

ARPA-E, 2012. Methane Opportunities for Vehicular Energy (MOVE), in http://arpa-e-foa.energy.gov (DE-FOA-000672).

Barin, G., Krungleviciute, V., Gomez-Gualdron, D.A., Sarjeant, A.A., Snurr, R.Q., Hupp, J.T., Yildirim, T., Farha, O.K., 2014. Isoreticular Series of (3,24)-Connected Metal–Organic Frameworks: Facile Synthesis and High Methane Uptake Properties. Chem. Mat. 26, 1912-1917.

Boys, S.F., Bernardi, F., 1970. The calculation of small molecular interactions by the differences of separate total energies. Some procedures with reduced errors. Mol. Phys. 19, 553-566.

Cavka, J.H., Jakobsen, S., Olsbye, U., Guillou, N., Lamberti, C., Bordiga, S., Lillerud, K.P., 2008. A New Zirconium Inorganic Building Brick Forming Metal Organic Frameworks with Exceptional Stability. J. Am. Chem. Soc. 130, 13850-13851.

Chen, B.; Siepmann, J. I., 1999. Transferable Potentials for Phase Equilibria. 3. Explicit-Hydrogen Description of Normal Alkanes. J. Phys. Chem. B 103, 5370–5379

Chen, L., Grajciar, L., Nachtigall, P., Düren, T., 2011. Accurate Prediction of Methane Adsorption in a Metal–Organic Framework with Unsaturated Metal Sites by Direct Implementation of an *ab Initio* Derived Potential Energy Surface in GCMC Simulation. J. Phys. Chem. C 115, 23074-23080.

Chung, Y.G., Camp, J., Haranczyk, M., Sikora, B.J., Bury, W., Krungleviciute, V., Yildirim, T., Farha, O.K., Sholl, D.S., Snurr, R.Q., 2014. Computation-Ready, Experimental Metal–Organic Frameworks: A Tool To Enable High-Throughput Screening of Nanoporous Crystals. Chem. Mat. 26, 6185-6192.

Clark, T., Chandrasekhar, J., Spitznagel, G.W., Schleyer, P.V.R., 1983. Efficient diffuse function-augmented basis sets for anion calculations. III. The 3-21+G basis set for first-row elements, Li–F. J. Comput. Chem. 4, 294-301.

Colón, Y.J., Fairen-Jimenez, D., Wilmer, C.E., Snurr, R.Q., 2014. High-Throughput Screening of Porous Crystalline Materials for Hydrogen Storage Capacity near Room Temperature. J. Phys. Chem. C 118, 5383-5389.

Coudert, F-.X., Boutin, A., Fuchs, A.H., Neymark, A.V., 2013, Adsorption Deformation and Structural Transitions in Metal-organic Frameworks: From Unit Cell to the Crystal. J. Phys. Chem. Lett. 4, 3198-3205

Deria, P., Gómez-Gualdrón, D.A., Bury, W., Schaef, H.T., Wang, T.C., Thallapally, P.K., Sarjeant, A.A., Snurr, R.Q., Hupp, J.T., Farha, O.K., 2015. Ultraporous, Water Stable, and Breathing Zirconium-Based Metal–Organic Frameworks with ftw Topology. J. Am. Chem. Soc. 137, 13183-13190.

Deria, P., Mondloch, J.E., Tylianakis, E., Ghosh, P., Bury, W., Snurr, R.Q., Hupp, J.T., Farha, O.K., 2013. Perfluoroalkane Functionalization of NU-1000 via Solvent-Assisted Ligand Incorporation: Synthesis and CO2 Adsorption Studies. J. Am. Chem. Soc. 135, 16801-16804.

Dubbeldam, D., Calero, S., Ellis, D.E., Snurr, R.Q., 2016. RASPA: molecular simulation software for adsorption and diffusion in flexible nanoporous materials. Mol. Sim. 42, 81-101.

Dunning Jr, T.H., Hay, P.J., 1977. Modern Theoretical Chemistry. Plenum, New York.

Düren, T., Sarkisov, L., Yaghi, O.M., Snurr, R.Q., 2004. Design of New Materials for Methane Storage. Langmuir 20, 2683-2689.

Eddaoudi, M., Kim, J., Rosi, N., Vodak, D., Wachter, J., O'Keeffe, M., Yaghi, O.M., 2002. Systematic Design of Pore Size and Functionality in Isoreticular MOFs and Their Application in Methane Storage. Science 295, 469-472.

Fei, H., Shin, J., Meng, Y.S., Adelhardt, M., Sutter, J., Meyer, K., Cohen, S.M., 2014. Reusable Oxidation Catalysis Using Metal-Monocatecholato Species in a Robust Metal–Organic Framework. J. Am. Chem. Soc. 136, 4965-4973.

Frisch, M.J., Pople, J.A., Binkley, J.S., 1984. Self-consistent molecular orbital methods 25. Supplementary functions for Gaussian basis sets. J. Chem. Phys. 80, 3265-3269.

Frisch, M.J., Trucks, G.W., Schlegel, H.B., Scuseria, G.E., Robb, M.A., Cheeseman, J.R., Scalmani, G., Barone, V., Mennucci, B., Petersson, G.A., Nakatsuji, H., Caricato, M., Li, X., Hratchian, H.P., Izmaylov, A.F., Bloino, J., Zheng, G., Sonnenberg, J.L., Hada, M., Ehara, M., Toyota, K., Fukuda, R., Hasegawa, J., Ishida, M., Nakajima, T., Honda, Y., Kitao, O., Nakai, H., Vreven, T., Montgomery Jr., J.A., Peralta, J.E., Ogliaro, F.o., Bearpark, M.J., Heyd, J., Brothers, E.N., Kudin, K.N., Staroverov, V.N., Kobayashi, R., Normand, J., Raghavachari, K., Rendell, A.P., Burant, J.C., Iyengar, S.S., Tomasi, J., Cossi, M., Rega, N., Millam, N.J., Klene, M., Knox, J.E., Cross, J.B., Bakken, V., Adamo, C., Jaramillo, J., Gomperts, R., Stratmann, R.E., Yazyev, O., Austin, A.J., Cammi, R., Pomelli, C., Ochterski, J.W., Martin, R.L., Morokuma, K., Zakrzewski, V.G., Voth, G.A., Salvador, P., Dannenberg, J.J., Dapprich, S., Daniels, A.D., Farkas, O., Foresman, J.B., Ortiz, J.V., Cioslowski, J., Fox, D.J., 2009. Gaussian 09. Gaussian, Inc., Wallingford, CT, USA.

Fu, J., Tian Y., Wu, Z., 2015. Seeking Metal-Organic Frameworks for Methane Storage in Natural Gas Vehicles. Adsorption 21, 499-507

Furukawa, H., Go, Y.B., Ko, N., Park, Y.K., Uribe-Romo, F.J., Kim, J., O'Keeffe, M., Yaghi, O.M., 2011. Isoreticular Expansion of Metal–Organic Frameworks with Triangular and Square Building Units and the Lowest Calculated Density for Porous Crystals. Inorg. Chem. 50, 9147-9152.

Gándara, F., Furukawa, H., Lee, S., Yaghi, O.M., 2014. High Methane Storage Capacity in Aluminum Metal–Organic Frameworks. J. Am. Chem. Soc. 136, 5271-5274.

Getman, R.B., Miller, J.H., Wang, K., Snurr, R.Q., 2011. Metal Alkoxide Functionalization in Metal−Organic Frameworks for Enhanced Ambient-Temperature Hydrogen Storage. J. Phys. Chem. C 115, 2066-2075.

Gómez Gualdrón, D.A., Balbuena, P.B., 2007. Classical Molecular Dynamics of Clathrate−Methane−Water−Kinetic Inhibitor Composite Systems†. J. Phys. Chem. C 111, 15554-15564.

Gómez-Gualdrón, D.A., Gutov, O.V., Krungleviciute, V., Borah, B., Mondloch, J.E., Hupp, J.T., Yildirim, T., Farha, O.K., Snurr, R.Q., 2014a. Computational Design of Metal–Organic Frameworks Based on Stable Zirconium Building Units for Storage and Delivery of Methane. Chem. Mat. 26, 5632-5639.

Gómez-Gualdrón, D.A., Wilmer, C.E., Farha, O.K., Hupp, J.T., Snurr, R.Q., 2014b. Exploring the limits of methane storage and delivery in nanoporous materials J. Phys. Chem. C 118, 6941-6915.

Grunker, R., Bon, V., Muller, P., Stoeck, U., Krause, S., Mueller, U., Senkovska, I., Kaskel, S., 2014. A new metal-organic framework with ultra-high surface area. Chem. Commun. 50, 3450-3452.

Hay, P.J., Wadt, W.R., 1985. Ab initio effective core potentials for molecular calculations. Potentials for K to Au including the outermost core orbitals. J. Chem. Phys. 82, 299-310.

He, Y., Zhou, W., Yildirim, T., Chen, B., 2013. A series of metal-organic frameworks with high methane uptake and an empirical equation for predicting methane storage capacity. Energy. Environ. Sci. 6, 2735-2744.

Head-Gordon, M., Pople, J.A., Frisch, M.J., 1988. MP2 energy evaluation by direct methods. Chem. Phys. Lett. 153, 503-506.

Karagiaridi, O., Bury, W., Mondloch, J.E., Hupp, J.T., Farha, O.K., 2014. Solvent-Assisted Linker Exchange: An Alternative to the De Novo Synthesis of Unattainable Metal–Organic Frameworks. Angew. Chem. Int. Ed. 53, 4530-4540.

Karra, J. R.; Walton, K. S. Effect of Open Metal Sites on Adsorption of Polar and Nonpolar Molecules in Metal−Organic Framework Cu-BTC, 2008. Langmuir, 24, 8620-8626.

Kim, M., Cohen, S.M., 2012. Discovery, development, and functionalization of Zr(IV)-based metal-organic frameworks. CrystEngComm 14, 4096-4104.

Koh, H. S.; Rana, M. K.; Wong-Foy, A. G.; Siegel, D. J., 2015. Predicting Methane Storage in Open-Metal-Site Metal–Organic Frameworks *J. Phys. Chem. C 119*, 13451-13458.

Krishnan, R., Binkley, J.S., Seeger, R., Pople, J.A., 1980. Self-consistent molecular orbital methods. XX. A basis set for correlated wave functions. J. Chem. Phys. 72, 650-654.

Li, B., Wen, H.-M., Wang, H., Wu, H., Tyagi, M., Yildirim, T., Zhou, W., Chen, B., 2014. A Porous Metal–Organic Framework with Dynamic Pyrimidine Groups Exhibiting Record High Methane Storage Working Capacity. J. Am. Chem. Soc. 136, 6207-6210.

Lucena, S. M. P.; Frutuoso, L. F. A.; Silvino, P. F. G.; Azevedo, D. C. S.; Toso, J. P.; Zgrablich, G.; Cavalcante, C. L., Jr., 2010. Molecular Simulation of Collection of Methane Isotherms in Carbon Material using all-atom and United Atom Models. Colloids Surf. A 357, 53–60.

Ma, S., Sun, D., Simmons, J.M., Collier, C.D., Yuan, D., Zhou, H.-C., 2007. Metal-Organic Framework from an Anthracene Derivative Containing Nanoscopic Cages Exhibiting High Methane Uptake. J. Am. Chem. Soc. 130, 1012-1016.

Ma, S., Zhou, H.-C., 2010. Gas storage in porous metal-organic frameworks for clean energy applications. Chem. Commun. 46, 44-53.

Martin, M.G., Siepmann, J.I., 1998. Transferable Potentials for Phase Equilibria. 1. United-Atom Description of n-Alkanes. J. Phys. Chem. B 102, 2569-2577.

Martin, R.L., Haranczyk, M., 2013. Insights into Multi-Objective Design of Metal–Organic Frameworks. Crys. Growth Des. 13, 4208-4212.

Martin, R.L., Lin, L.-C., Jariwala, K., Smit, B., Haranczyk, M., 2013. Mail-Order Metal–Organic Frameworks (MOFs): Designing Isoreticular MOF-5 Analogues Comprising Commercially Available Organic Molecules. J. Phys. Chem. C 117, 12159-12167.

Martin, R.L., Simon, C.M., Medasani, B., Britt, D.K., Smit, B., Haranczyk, M., 2014a. In Silico Design of Three-Dimensional Porous Covalent Organic Frameworks via Known Synthesis Routes and Commercially Available Species. J. Phys. Chem. C 118, 23790-23802.

Martin, R.L., Simon, C.M., Smit, B., Haranczyk, M., 2014b. In silico Design of Porous Polymer Networks: High-Throughput Screening for Methane Storage Materials. J. Am. Chem. Soc. 136, 5006-5022.

Mason, J.A., Oktawiec, J., Taylor, M.K., Hudson, M.R., Rodriguez, J., Bachman, J.E., Gonzalez, M.I., Cervellino, A., Guagliardi, A., Brown, C.M., Llewellyn, P.L., Masciocchi, N., Long, J.R., 2015. Methane storage in flexible metal–organic frameworks with intrinsic thermal management. Nature 527, 357-361.

Mason, J.A., Veenstra, M., Long, J.R., 2014. Evaluating metal-organic frameworks for natural gas storage. Chem. Sci. 5, 32-51.

McDaniel, J.G., Li, S., Tylianakis, E., Snurr, R.Q., Schmidt, J.R., 2015, Evaluation of Force Field Performance for High-Throughput Screening of Gas Uptake in Metal-Organic Frameworks, J. Phys. Chem. C 119, 3143-3152

McLean, A.D., Chandler, G.S., 1980. Contracted Gaussian basis sets for molecular calculations. I. Second row atoms, Z=11–18. J. Chem. Phys. 72, 5639-5648.

Mondloch, J.E., Bury, W., Fairen-Jimenez, D., Kwon, S., DeMarco, E.J., Weston, M.H., Sarjeant, A.A., Nguyen, S.T., Stair, P.C., Snurr, R.Q., Farha, O.K., Hupp, J.T., 2013. Vapor-Phase Metalation by Atomic Layer Deposition in a Metal–Organic Framework. J. Am. Chem. Soc. 135, 10294-10297.

Nicholson, D., Parsonage, N.G., 1982. Computer simulation and the statistical mechanics of adsorption. Academic Press, London.

Peng, Y., Krungleviciute, V., Eryazici, I., Hupp, J.T., Farha, O.K., Yildirim, T., 2013. Methane Storage in Metal–Organic Frameworks: Current Records, Surprise Findings, and Challenges. J. Am. Chem. Soc. 135, 11887-11894.

Raksakoon, C., Maihom, T., Probst, M., Limtrakul, J., 2015. Hydration of Carbon Dioxide in Copper-Alkoxide Functionalized Metal–Organic Frameworks: A DFT Study. J. Phys. Chem. C 119, 3564-3571.

Ramsey, W.H., 1963. On the densities of methane, metallic ammonium, water and neon at planetary pressures. Mon. Not. R. Atron. Soc. 125, 469-485.

Rana, M.K., Koh, H.S., Zuberi, H., Siegel, D.J., 2014. Methane Storage in Metal-Substituted Metal–Organic Frameworks: Thermodynamics, Usable Capacity, and the Impact of Enhanced Binding Sites. J. Phys. Chem. C 118, 2929-2942.

Rappe, A.K., Casewit, C.J., Colwell, K.S., Goddard, W.A., Skiff, W.M., 1992. UFF, a full periodic table force field for molecular mechanics and molecular dynamics simulations. J. Am. Chem. Soc. 114, 10024-10035.

Schneemann, A., Bon, V., Schwedler, I., Senkovska, I., Kaskel, S., Fischer, R.A., 2014. Flexible metal-organic frameworks. Chem. Soc. Rev. 43, 6062-6096.

Sezginel, K.B., Uzun, A., Keskin, S., 2015. Multivariable linear models of structural parameters to predict methane uptake in metal–organic frameworks. Chemical Engineering Science 124, 125-134.

Simon, C.M., 2015. https://github.com/CorySimon/EmptyBox. (*accessed Nov. 2015*).

Simon, C.M., Kim, J., Gomez-Gualdron, D.A., Camp, J.S., Chung, Y.G., Martin, R.L., Mercado, R., Deem, M.W., Gunter, D., Haranczyk, M., Sholl, D.S., Snurr, R.Q., Smit, B., 2015. The materials genome in action: identifying the performance limits for methane storage. Energy. Environ. Sci. 8, 1190-1199.

Simon, C.M., Kim, J., Lin, L.-C., Martin, R.L., Haranczyk, M., Smit, B., 2014. Optimizing nanoporous materials for gas storage. Phys. Chem. Chem. Phys. 16, 5499-5513.

Sloan, E.D., 2003. Fundamental principles and applications of natural gas hydrates. Nature 426, 353-363.

Sun, Y.; Spellmeyer, D.; Pearlman, D. A.; Kollman, P. Simulation of the Solvation Free Energies for Methane, Ethane, and Propane and Corresponding Amino Acid Dipeptides: A Critical Test of the Bond-PMF Correction, A new Set of Hydrocarbon Parameters, and the Gas Phase-water Hydrophobicity Scale. J. Am. Chem. Soc. 1992, 114, 6798–6801.

Tanabe, K.K., Allen, C.A., Cohen, S.M., 2010. Photochemical Activation of a Metal–Organic Framework to Reveal Functionality. Angew. Chem. Int. Ed. 49, 9730-9733.

Uzun, A.; Keskin, S., 2014. Site Characteristics in Metal Organic Frameworks for Gas Adsorption Progress in Surface Science 89, 56-79.

Wang, T.C., Bury, W., Gomez-Gualdron, D.A., Vermeulen, N.A., Mondloch, J.E., Deria, P., Zhang, K., Moghadam, P.Z., Sarjeant, A.A., Snurr, R.Q., Stoddart, J.F., Hupp, J.T., Farha, O.K., 2015. Ultrahigh Surface Area Zirconium MOFs and Insights into the Applicability of the BET Theory. J. Am. Chem. Soc.

Wen, H.-M., Li, B., Yuan, D., Wang, H., Yildirim, T., Zhou, W., Chen, B., 2014. A porous metal-organic framework with an elongated anthracene derivative exhibiting a high working capacity for the storage of methane. J. Mat. Chem. A 2, 11516-11522.

Weston, M.H., Farha, O.K., Hauser, B.G., Hupp, J.T., Nguyen, S.T., 2012. Synthesis and Metalation of Catechol-Functionalized Porous Organic Polymers. Chem. Mat. 24, 1292-1296.

Wilmer, C.E., Farha, O.K., Yildirim, T., Eryazici, I., Krungleviciute, V., Sarjeant, A.A., Snurr, R.Q., Hupp, J.T., 2013. Gram-scale, high-yield synthesis of a robust metal-organic framework for storing methane and other gases. Energy. Environ. Sci. 6, 1158-1163.

Wu, H., Zhou, W., Yildirim, T., 2009. High-Capacity Methane Storage in Metal−Organic Frameworks M_2(dhtp): The Important Role of Open Metal Sites. J. Am. Chem. Soc. 131, 4995-5000.

Yuan, D., Zhao, D., Sun, D., Zhou, H.-C., 2010. An Isoreticular Series of Metal–Organic Frameworks with Dendritic Hexacarboxylate Ligands and Exceptionally High Gas-Uptake Capacity. Angew. Chem. Int. Ed. 49, 5357-5361.

Zhang, H., Deria, P., Farha, O.K., Hupp, J.T., Snurr, R.Q., 2015. A thermodynamic tank model for studying the effect of higher hydrocarbons on natural gas storage in metal-organic frameworks. Energy Environ. Sci. 8, 1501-1510.

Zhou, W., Wu, H., Hartman, M.R., Yildirim, T., 2007. Hydrogen and Methane Adsorption in Metal−Organic Frameworks: A High-Pressure Volumetric Study. J. Phys. Chem. C 111, 16131-16137.